



Effect of cutting parameters on surface residual stresses in dry turning of AISI 1035 alloy

K. h. Salman¹ · Ammar H. Elsheikh^{2,3} · M. Ashham¹ · Mohammed Kamal Ahmed Ali⁴ · Maher Rashad² · Zhang Haiou³

Received: 26 March 2019 / Accepted: 8 July 2019 / Published online: 2 August 2019
© The Brazilian Society of Mechanical Sciences and Engineering 2019

Abstract

Residual stresses (RSes) induced by turning processes have a great effect on the material properties of the machined components and their abilities to withstand severe loading conditions (creep, fatigue, and stress corrosion cracking). The final state of RSes in a workpiece depends on its material and on the employed cutting parameters/conditions such as cutting speed, depth of cut, feed speed, cutting tool geometry, wear of the tool, cutting tool geometry, cutting tool coating, and cooling. This study introduces a comprehensive investigation of the effects of different cutting parameters, such as cutting speed (30, 60, and 90 m/min), feed (0.05, 0.1, and 0.3 mm/rev), and depth of cut (0.1, 0.5, and 1 mm) as well as cutting tool geometry such as cutting tool nose radius (0.397, 0.794, and 1.191 mm), and cutting tool coating (coated and uncoated) on the cutting force, maximum cutting temperature, surface microstructure, and surface residual stresses during cutting AISI 1035 alloy steel. The RSes were measured using X-ray diffraction technique. The experiments were designed using Taguchi method based on L_{18} orthogonal array, and the significance level of different cutting parameters as well as cutting tool properties have been determined via applying analysis of variance. Numerical simulations have been carried out using commercial machining software AdvantEdge.

Keywords Machining · Turning · Residual stresses · Taguchi · ANOVA · AdvantEdge

1 Introduction

The quality and the functional behavior of the machined components are greatly affected by the induced residual stresses (RSes) state in the surface and subsurface layers. Depending on the attributes of the induced RSes state, RSes

can be either beneficial (compressive RSes) or detrimental (tensile RSes) to the performance of machined components [1]. It is well known that tensile RSes in the surface and subsurface layers are usually detrimental to fatigue life [2], creep life [3], and stress corrosion cracking resistance [4], while compressive RSes are usually beneficial to the same properties [5]. Many attempts have been done to figure out the relationship between different cutting parameters/conditions and the induced RSes using experimental [6–8], analytical modeling [9–11], finite element modeling [12–14], and various combinations of them [15–17] in various machining operations [18–20]. The experimental investigations were carried out via measuring the RSes using different measuring methods such as ring core method [21], hole drilling technique [22], deep-hole drilling [23], slope cutting method [24], contour method [25], synchrotron diffraction [26] method, XRD method [27], and neutron diffraction method [28]. Among all these measuring techniques, XRD and hole drilling technique are the most commonly used in machining applications. The XRD technique is widely used nondestructive technique that is used to measure high-magnitude RSes

Technical Editor: Lincoln Cardoso Brandao.

✉ Ammar H. Elsheikh
ammar_elsheikh@f-eng.tanta.edu.eg

¹ Mechanical Department, Kut Technical Institute, Middle Technical University, Baghdad 10074, Iraq

² Production Engineering and Mechanical Design Department, Faculty of Engineering, Tanta University, Tanta 31521, Egypt

³ State Key Laboratory of Digital Manufacturing Equipment and Technology, Huazhong University of Science and Technology, Wuhan 430074, China

⁴ Automotive and Tractors Engineering Department, Faculty of Engineering, Minia University, El-Minia 61111, Egypt

of polycrystalline materials with reasonable accuracy. It is also very quick and easy to apply the process and therefore cheap. Therefore, it has been chosen to measure RSEs in this study. On the other hand, commercial finite element analysis (FEA) software as a powerful numerical modeling technique has been used to determine the RSEs state in different machining operations; the most commonly used softwares are DEFORM [29], ABAQUS [30], and AdvantEdge [31].

Pawade et al. [32] investigated the effect of cutting parameters and tool geometry on surface RSEs during turning of Inconel 718 using XRD method. Capello [33] carried out an experimental investigation on the effects of the workpiece material and cutting parameters on the induced surface RSEs in turning process using XRD as a measuring technique. The obtained results revealed that feed rate and nose radius have the greatest effect on the RSEs state, while the depth of cut has a negligible effect on the RSEs. In another study, Tsuchida et al. [34] reported that depth of cut has negligible effect on the RSEs, while controlling feed rate can move the RSEs from tensile to compressive state. Gunnberg et al. [35] reported an increase in the surface tensile RSEs with increasing the cutting speed, an increase in compressive stresses with increasing the feed rate, and a negligible effect of cutting depth on the RSEs state during turning of 18MnCr5 case-carburized steel. Contrary to these finding, Saini et al. [36] found that the depth of cut and feed rate have the greatest effect on RSEs state while nose radius and cutting speed have mild effect on it. The experiments were carried out on AISI H11 tool steel turned using ceramic tools, and the RSEs were measured using XRD technique. Liu et al. [37] investigated the effects of tool nose radius and tool wear on the RSEs state during turning of JIS SUJ2 bearing steel. They reported that the induced surface RSEs state becomes more tensile by increasing tool wear and the tool nose radius. Furthermore, they found that the effect of the nose radius on the RSEs state is diminished by increasing the tool wear. Outeiro et al. [38] investigated the effect of coating condition on the RSEs state during turning of AISI 316L and AISI 1045 steels. They reported that: cutting with coated tools results in higher tensile RSEs compared with uncoated tools due to the increase in the workpiece temperature in the case of coated tool compared with uncoated tool.

Numerical modeling using FEA has shown promising capabilities in predicting RSEs without conducting costly experiments. However, it suffers from the computational costs as well as the convergence and uncertainty problems associated with elastic–viscoplastic deformations [39]. Outeiro et al. [40] used DEFORM-2D as an elastic–viscoplastic FEA software to predict the RSEs state in orthogonal cutting of AISI 316L steel. Ozel and Ulutan [29] used DEFORM-3D, as a three-dimensional updated Lagrangian-based FEA software, to predict the RSEs during turning Ti–6Al–4V and IN100 alloys. Liu and Guo [30] used ABAQUS as an

explicit FEA software to investigate the effect of sequential cuts and tool-chip friction on RSEs state during machining AISI 304 stainless steel. Kundrák et al. [41] determined the RSEs state in the machined surface at different cutting tool geometries using “Third Wave AdvantEdge™ 5.9 2D” FEA software which possess a high computational capability in different machining operations with a very user-friendly interface. Both of Lagrangian formulation and explicit time integration are implemented in AdvantEdge to simulate two- or three-dimensional metal cutting processes.

There is a great diversity in the results reported in the previous studies conducted on RSEs due to measurements and computational modeling difficulties, as well as dissimilar cutting conditions, tool parameters and workpiece materials, while many studies claim that RSEs created during turning have tensile nature [42–44], some claim that they are compressive [45–47]. Moreover, the results reported in literature show discrepant effect of different cutting parameters/conditions on the final RSEs state. Therefore, more studies are needed to investigate the effects of different cutting parameters/conditions on the induced RSEs in turning operations for different materials. Moreover, optimization-based investigations should be carried out to select the optimal cutting conditions and predict the process responses using artificial intelligence and advanced optimization techniques such as artificial neural networks [48–50], adaptive neuro-fuzzy inference system [51, 52], ant colony optimization [53, 54], crow search algorithm [55], particle swarm optimization [56–58], and other metaheuristic techniques [59]. There are three main reasons contributing to the final state of RSEs [60]:

- The pressure acting at the workpiece from the tool produces plastic deformation of the workpiece which results in compressive RSEs (mechanical effect is dominant).
- Plastic deformation of the workpiece and chips as well as the friction between the tool and the workpiece leads to overheating of the workpiece. The variation between the temperature of workpiece surface and the bulk workpiece material results in tensile RSEs after cooling (thermal effect is dominant).
- High cutting temperature may result in phase transformations for some materials causing volumetric changes in the workpiece material and consequently compressive RSEs are generated.

Based on the domination of thermal, mechanical, or phase transformation effects, the final state of RSEs may be tensile or compressive depending on the mechanical, thermal, and physical properties of the machined material as well as the employed cutting parameters/conditions.

The previous investigations were focused on correlating different cutting parameters (depth of cut, feed rate, and

cutting speed), cutting tool geometry (nose radius and rake angle), and cutting conditions (wet and dry cutting) with the final state of RSEs induced in the machined components. Various metal alloys have been investigated in the literature such as steel alloys (AISI 1045 and AISI 4340 steel [61], AISI 52100 steel [62], AISI 304 stainless steel [63], AISI 316L steels [38], AISI H11 tool steel [34], JIS SUJ2 bearing steel [37], and UNI-ISO 39NiCrMo3 and UNI-ISO C45 steels [64]), titanium alloys (Ti-6246 and Ti-64 [65]), and nickel–chromium-based superalloys (Inconel 718 [66], RR1000 nickel-based superalloy [67], 18MnCr5 [35], and 34CrNiMo6 [68]). In this paper, the effects of different cutting parameters/conditions such as coating condition, tool nose radius, cutting speed, feed rate, and cutting depth on the induced RSEs during machining of AISI 1035 alloy are investigated. This type of steel is commonly used in manufacturing of couplings, links, gears, axles, and shafts. However, for the best of authors' knowledge, there is no previous investigation carried out on the induced RSEs during turning of this alloy. The main purpose of this experimental study is to figure out the significance and effects of different cutting parameters during turning AISI 1035 alloy on the hardness, microstructure, and surface residual stresses of the machined workpieces under dry cutting conditions.

2 Experimental work

2.1 Work material

Cylindrical specimens (40 mm diameter and 150 mm length) were cut from an AISI 1035 round bar with mechanical properties presented in Table 1. The chemical composition of the examined steel given in Table 2 was determined by means of mass spectrometry using a multi-channel optical emission spectrometer device (ARL 3460 model metals analyzer). The microstructure of as-received AISI 1035 containing pearlite and ferrite phases is shown in Fig. 1.

Table 1 Mechanical properties of AISI 1035 carbon steel [69]

Yield strength (MPa)	Ultimate tensile strength (Mpa)	Shear yield strength (MPa)	Ultimate shear strength (MPa)	Elongation (%)	Hardness (Hv)
550	620	339.8	406.8	13	188

Table 2 Chemical composition of AISI 1035 carbon steel in weight (wt.) percentage

	Fe	C	Si	S	P	Mn
Measured	Bal.	0.35	0.21	0.026	0.011	0.64
Standard [70]	Bal.	0.32–0.38	0.07–0.6	0.050 max	0.040 max	0.60–0.90

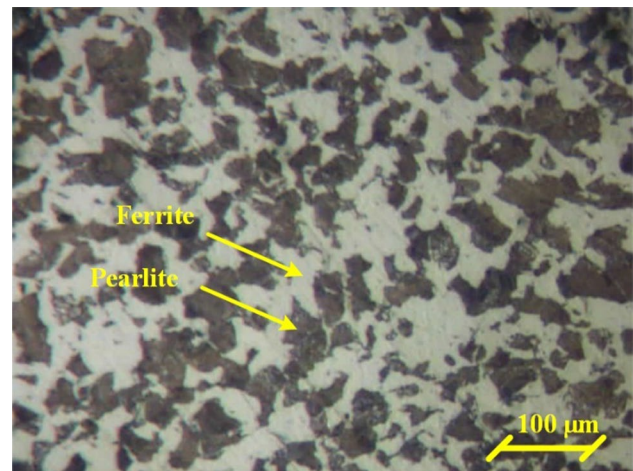


Fig. 1 Microstructures of as-received AISI 1035

2.2 Experimental procedures

The turning experiments were performed on Knuth Starchip 450 CNC Lathe with a hydraulic power chuck and a constant cutting speed control system under dry cutting conditions using DTGNL 16 3D SANDVIK tool holder with 25.4 mm shank width and WNMG 08 04 XX-PF 4315 carbide cutting insert, where XX is the designation of the tool radius (04 for 0.397 mm 08 for 0.794 mm, and 12 for 1.191 mm) as shown in Fig. 2. The main purpose of this experimental study is to figure out the significance and effects of different cutting parameters on the hardness, microstructure, and surface residual stresses of the machined workpieces under dry cutting conditions. Zwick & Co Z323 hardness tester was used to measure hardness values of the machined workpieces surfaces with 0.9 kg load. Hardness value for each specimen is the average of three measurements on the machined surface. The microstructure of the specimens was observed using optical microscopy (Olympus SZ61). The specimen surfaces have been first wet ground with 600, 1200 grit SiC papers and polished with 1, 0.3, 0.1 μm alumina powder on Metaserv rotary pre-grinder polisher. Then, the contamination on the polished surfaces was removed using ultrasonic machine. Finally, the polished surfaces are etched by 2% Nital (nitric acid and alcohol solution) to expose the grain structure and morphology. The machined surface residual stress state was analyzed by X-ray diffraction technique (XRD) by applying $\sin^2\psi$ method using LabX XRD-6000 X-ray Diffractometer [71]. Medium carbon steel chromium (Cr K- α) X-ray anode tube was used to acquire the

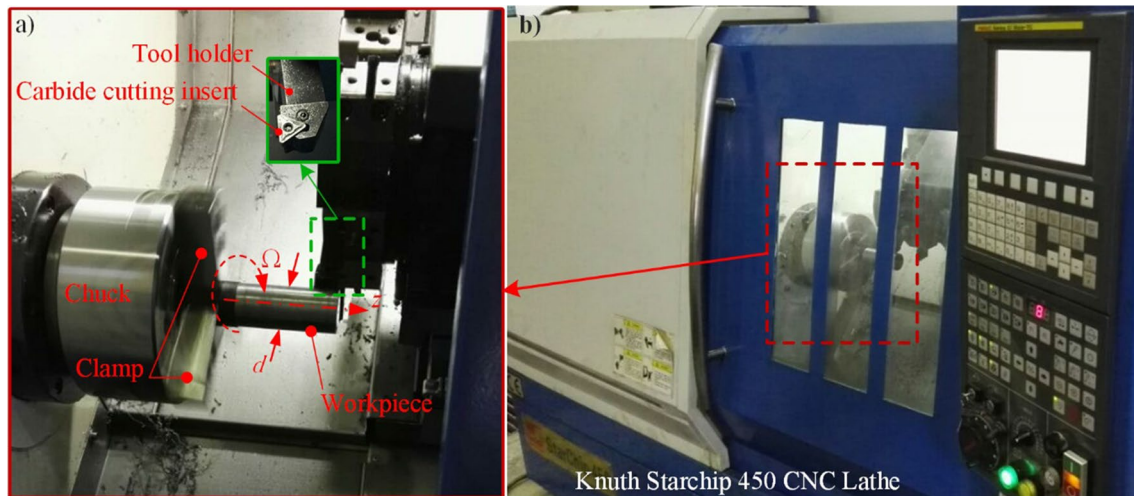


Fig. 2 Experimental setup

Table 3 Measurement conditions of X-ray diffraction

Voltage (kV)	Intensity (mA)	Pinhole (mm)	Detector slit (mm)	2θ range ($^{\circ}$)	Step size ($^{\circ}$)	Scan speed (step/s)	K -Constant (MPa/ $^{\circ}$)
40	40	2	0.4	150–162	0.1	2	– 32.44

(2 1 1) diffraction peak at a Bragg angle of about 156° with four different orientations of the sample surface (0° , 15° , 30° , and 45°), using a spot size of 1 mm in diameter. The Poisson's ratio and Young's modulus used for the (2 1 1) reflection were 0.27 and 210 GPa, respectively. The measurement parameters used for the X-ray diffraction measurements are summarized in Table 3. Moreover, numerical simulations were carried out on commercial FEA software AdvantEdge to calculate important machining parameters such as cutting forces, heat generated, temperatures, strains, and stresses prior to real cutting process [72]. These simulations ensure achieving optimized cutting conditions with remarkable reduction of the cost.

2.3 Experimental design

Taguchi method, as a design of experiments technique, is used to model and analyze the influence of different parameters on the hardness, microstructure, and surface residual stresses of the machined workpieces. The orthogonal arrays design used in this method provides a reasonable reduction of experimental number via distributing the variables in a balanced manner, thus greatly reducing the number of experiments required. Five factors are used in this investigation, namely type of coating, nose radius, cutting speed, feed rate, and depth of cut. The first factor has two levels, while the remaining factors have three levels. The investigated factors and their levels are listed in Table 4. L_{18} orthogonal array with a mixed design (one factor with two levels and four

Table 4 Cutting parameters and their levels

Factor	Factor identifier	Level 1	Level 2	Level 3
Type of coating	A	Uncoated	Coated	
Nose radius (mm)	B	0.397	0.794	1.191
Cutting speed (m/min)	C	30	60	90
Feed rate (mm/rev)	D	0.05	0.1	0.3
Depth of cut (mm)	E	0.1	0.5	1

factors with three levels in eighteen runs of experiments) is implemented. Orthogonal array with eighteen rows represents the number of the runs (the number of experiments) as shown in Table 5. Eighteen experiments were conducted using fresh uncoated and CVD TiCN + Al_2O_3 + TiN-coated carbide-cutting tool to avoid the tool wear effect on the obtained results.

3 Results and discussion

The main obtained results from the experiments and simulations based on the experimental design in the previous section are given in Table 6. A brief discussion of the results is presented in the next subsections. As the experiment No. 13 has the worst results in terms of RSEs and generated heat, the simulation results of that experiment (including,

Table 5 Taguchi L_{18} orthogonal array

Experiment no.	Cutting parameter level				
	A	B	C	D	E
1	A1	B1	C1	D2	E3
2	A1	B1	C2	D3	E1
3	A1	B1	C3	D1	E2
4	A2	B1	C1	D1	E2
5	A2	B1	C2	D2	E3
6	A2	B1	C3	D3	E1
7	A1	B3	C1	D3	E2
8	A1	B3	C2	D1	E3
9	A1	B3	C3	D2	E1
10	A2	B3	C1	D2	E1
11	A2	B3	C2	D3	E2
12	A2	B3	C3	D1	E3
13	A1	B2	C1	D3	E3
14	A1	B2	C2	D1	E1
15	A1	B2	C3	D2	E2
16	A2	B2	C1	D1	E1
17	A2	B2	C2	D2	E2
18	A2	B2	C3	D3	E3

employed mesh, the rate of the generated heat, temperature, strain rate, induced plastic strain, and induced Mises stress) are plotted in Fig. 3. A finer mesh is employed at the cutting zone as shown in Fig. 3a to compensate the high-temperature

gradient and strain rates, while coarser mesh is employed far away from the cutting zone to decrease the computational costs. The simulation results indicate that high heat rates of 1.5 KW/mm^3 were generated during cutting process at cutting zone which results in elevated cutting zone temperature up to more than $230 \text{ }^\circ\text{C}$. Moreover, very high strain rates were observed in the cutting zone that reached 1500 s^{-1} with peak plastic strain and Mises stress of 4 and 1000 MPa, respectively.

3.1 Cutting forces

During turning, the resultant force from the cutting operation can be decomposed into three main components: main cutting force (F_c) acts in the direction of the main primary motion (cutting direction), feed force (F_f) acts in the feed direction, and passive force (F_p) acts in the direction of the depth of cut. The resultant force (F) can be calculated using the following equation:

$$F = \sqrt{F_c^2 + F_f^2 + F_p^2}$$

The determination of these forces is of great importance as they are responsible for power consumption and heat generation in the cutting zone as well as surface roughness and the geometrical accuracy of the machined surface. Figure 4 shows the plot of the simulation results of cutting force, feed force, and passive forces, power, torque, and temperature,

Table 6 Experimental results

Experiment no.	Cutting parameter level						
	F_x (N)	F_y (N)	F_z (N)	T_{max} ($^\circ\text{C}$)	Average grain diameter (mm)	Hardness HV (kg/mm^2)	Residual stresses (MPa)
1	-227.09	133.60	67.75	125.893	0.048	178.60	186.251
2	-81.126	16.36	50.34	174.638	0.037	181.09	219.566
3	-70.28	75.33	44.18	159.924	0.033	164.69	-64.046
4	-69.30	80.52	52.47	102.924	0.035	160.41	133.510
5	-235.97	132.65	59.87	191.603	0.032	194.35	239.924
6	-88.94	16.13	54.41	209.493	0.042	248.20	240.443
7	-265.52	51.85	108.20	228.800	0.030	166.89	330.320
8	-134.65	132.63	113.10	210.639	0.028	200.07	244.895
9	-38.22	7.11	32.218	170.351	0.032	252.29	52.211
10	-36.28	6.207	31.05	92.7116	0.028	188.88	139.796
11	-271.17	46.41	92.08	299.524	0.042	154.30	319.334
12	-134.22	134.57	111.61	219.6	0.032	152.34	317.440
13	-506.25	116.08	129.33	219.92	0.042	143.08	361.872
14	-22.04	6.15	24.07	114.066	0.045	137.93	65.473
15	-146.80	83.24	109.69	228.473	0.039	162.53	211.320
16	-20.83	6.07	22.96	81.5306	0.032	360.93	107.837
17	-143.89	88.53	110.78	182.968	0.035	197.18	161.265
18	-558.69	128.16	138.45	298.690	0.037	194.35	338.569

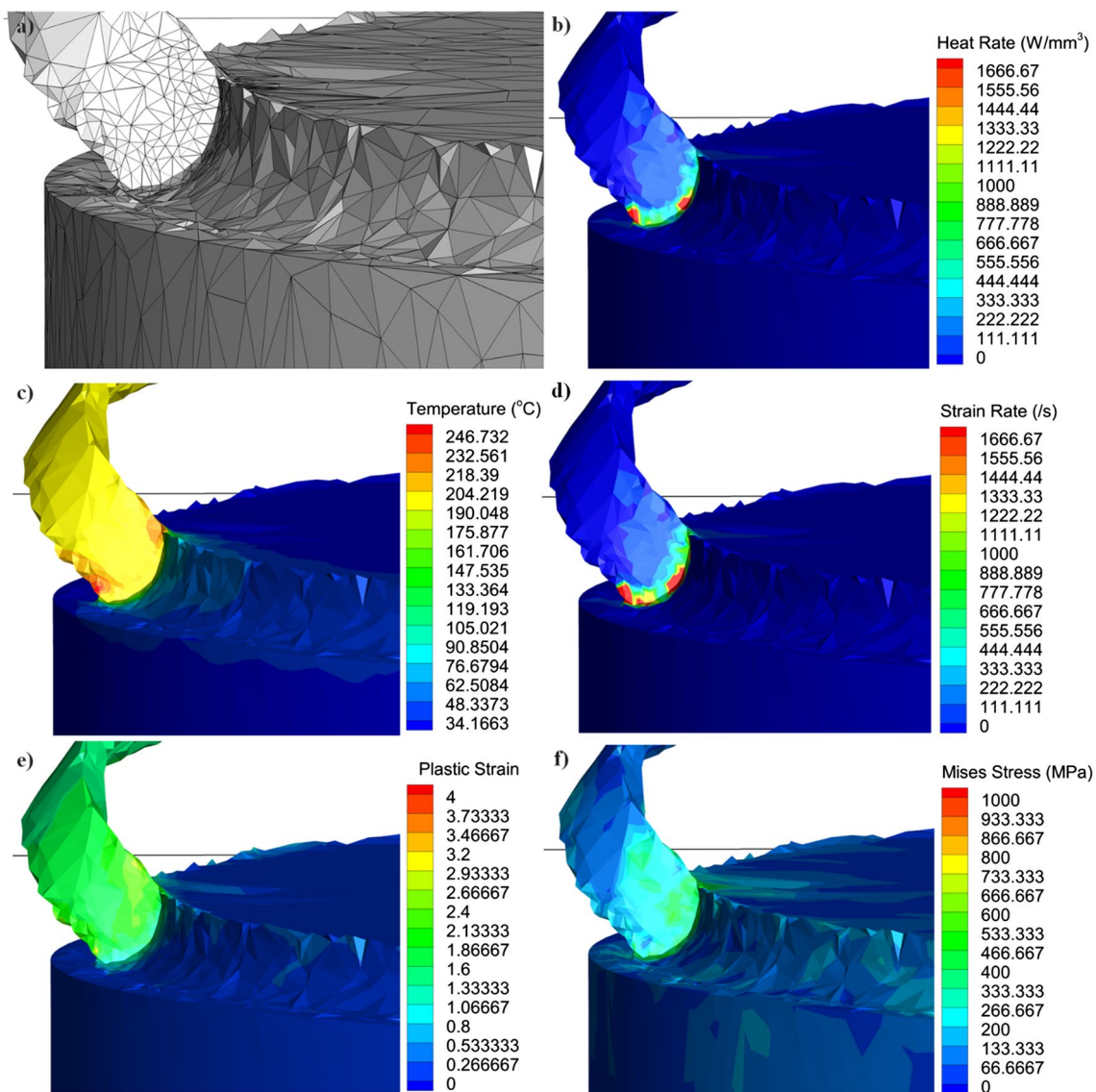


Fig. 3 Simulation results of the experiment No. 13: **a** employed mesh; **b** the rate of the generated heat; **c** temperature; **d** strain rate; **e** induced plastic strain; **f** induced Mises stress

with time of the experiment No. 13. From that figure, it can be observed that the cutting force has higher values than passive and feed forces, and both of the torque and the power have a periodic nature. That is due to lead angle effect which is considered as a determinant factor in interrupted turning due to the intermittent hitting [73]. Figure 5 plotted the effect of different investigated factors (coating condition, nose radius, cutting speed, feed rate, and cutting depth) on the resultant force as well as the force components. The plotted results indicate that the depth of cut has a dominant effect on all force components, while the coating condition has a negligible effect on all force components. Moreover, the feed rate as well as depth of cut has a significant effect on the main cutting force. More precisely, the Pearson

correlation coefficient and the p value between the resultant force and different cutting parameters are (0.025, 0.061, -0.008 , 0.534, and 0.771) and (0.920, 0.810, 0.976, 0.022, and 0.001) for coating condition, nose radius, cutting speed, feed rate, and depth of cut, respectively, which indicates the significant effect of the depth of cut followed by the feed rate on the resultant force, while the coating condition, nose radius, and the cutting speed have a negligible correlation with the resultant force (with p values of 0.920, 0.810, and 0.976 which are greater than the significance level of 0.05). Moreover, the covariance analysis indicates that while the resultant force increases with the increase in the depth of cut and the feed rate, it decreases with the increase in the cutting

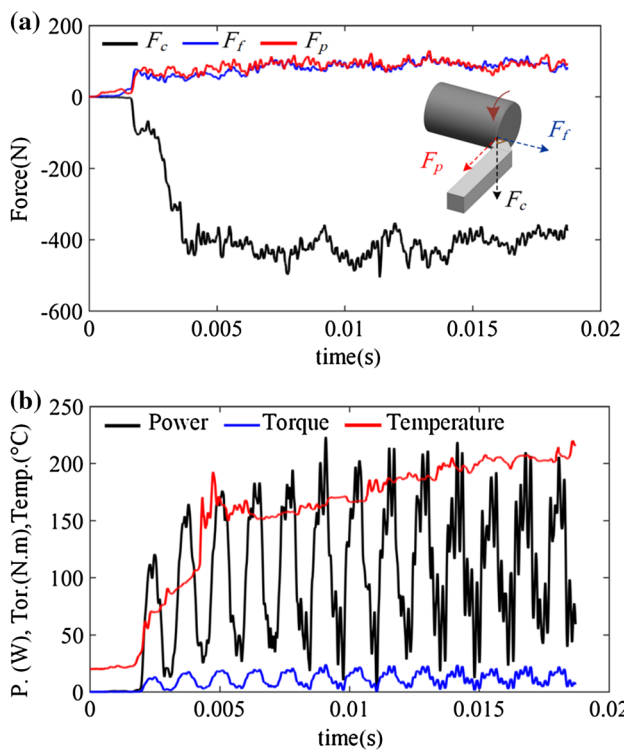


Fig. 4 Simulation results of the experiment No. 13: **a** cutting, feed and passive forces; **b** power, torque, and temperature

speed. The same effect of the different cutting parameters is observed for the main cutting force.

3.2 Cutting temperature

The feed rate has the most significant effect on the maximum workpiece temperature followed by cutting speed, depth of cut, and nose radius, while coating condition has a moderate effect on the maximum workpiece temperature as shown in Fig. 6a. More precisely, the Pearson correlation coefficient and the p value between the maximum generated temperature and different cutting parameters are (0.042, 0.283, 0.478, 0.633, and 0.453) and (0.870, 0.256, 0.045, 0.005, and 0.059) for coating condition, nose radius, cutting speed, feed rate, and depth of cut, respectively, which indicate the significant effect of the feed rate followed by the cutting speed on the maximum generated temperature, while the depth of cut has a moderate effect on the maximum generated temperature. Coating conditions and nose radius have a negligible correlation with the maximum generated temperature (with p values of 0.870 and 0.256 which are greater than the significance level of 0.05). Moreover, the covariance analysis indicates that the temperature increases with increasing the nose radius, cutting speed, feed rate, and depth of cut and also increase with the use of coating tools.

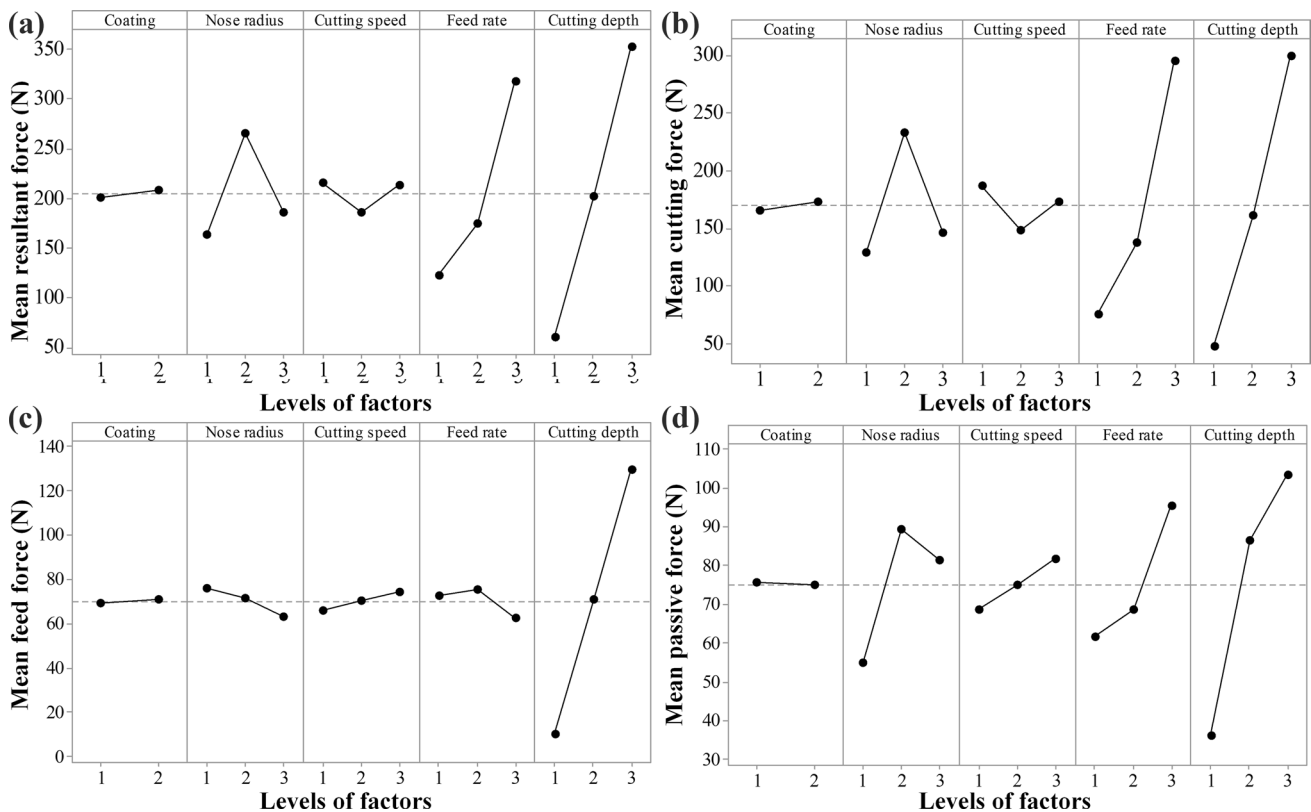
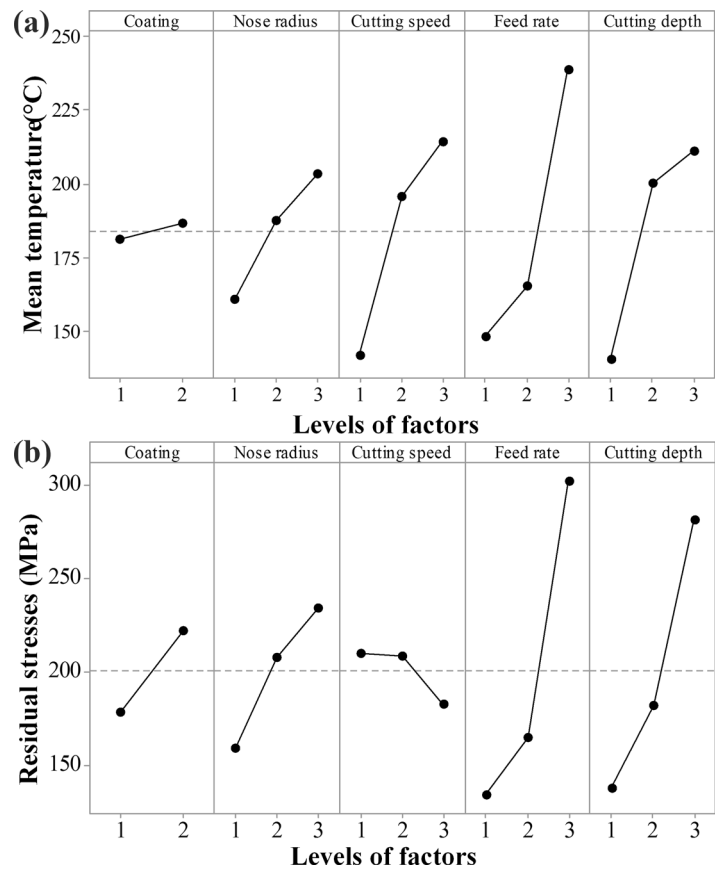


Fig. 5 Effect of different factors means on: **a** resultant force; **b** cutting force; **c** feed force; **d** passive force

Fig. 6 Effect of different factors means on the maximum temperature



The increase in the temperature with the increase in the nose radius is due to the increase in the contact area between tool and workpiece which results in more frictional heat generation [74]. The increase in the temperature in case of coated tools is because the coating acts as a thermal barrier, leading to more heat transferred into the workpiece [61, 75].

On the other hand, the Pearson correlation coefficient and the p value between the maximum generated temperature and different force components are (0.688, 0.394, and 0.777) and (0.002, 0.106, and 0.001) for main cutting force, feed force, and passive force, respectively, which indicates the significant effect of the main cutting force followed by the passive force on the maximum generated temperature, while the feed force has a negligible correlation with the maximum generated temperature (with p value of 0.106 which is greater than the significance level of 0.05).

3.3 Surface microstructure

During the cutting process of the steel, the machined surface may undergo microstructural changes due to the high local cutting temperature and/or severe mechanical deformation [76]. As the maximum cutting temperature for all conducted experiments does not exceed the austenitizing temperature (830–860 °C), there is no significant change in

the workpiece microstructure in terms of average grain size. p value between the average grain diameter and the coating condition, nose radius, cutting speed, feed rate, and depth of cut was 0.440, 0.074, 0.979, 0.216, and 0.876, respectively. The high values of p values indicate the negligible effect of coating condition, cutting speed, feed rate, and depth of cut on the average grain diameter of the machined workpieces. The lower p value between the nose radius and the average grain diameter, however it is greater than the significance level of 0.05 which considered in this study, indicates the moderate correlation between them, due to the increase of plowing force with the increase in nose radius which in consequence results in dominance mechanical effects and mechanical grain [32].

3.4 Surface hardness

The surface hardness does not show significant changes from the base material due to the moderate level of the cutting temperature. The p values of the surface hardness with coating condition, nose radius, cutting speed, feed rate, and depth of cut were 0.250, 0.948, 0.899, 0.602, and 0.114, respectively, which reveal the insignificant effect of different cutting parameters on the surface hardness. Moreover, the results of the covariance analysis reveal that the further

increase in nose radius, cutting speed, feed rate, and depth of cut may result in decrease in the workpiece hardness due to the increase in the cutting temperature with the increase of those parameters.

3.5 Surface residual stresses

In this section, the effects of different investigating factors on the generated residual stresses on the workpiece surface are investigated. The results from the conducted experiments, based on the covariance analysis, reveal that the increase in the nose radius, feed rate, and depth of cut as well as using a coated tool results in more tensile residual stresses, while the increase in the cutting speed results in decrease in the magnitude of the tensile residual stresses. These effects of different investigated factors on the surface residual stresses can be examined as follows:

- Coating condition: the coated tools produces more tensile surface residual stresses, because the coating acts as a thermal barrier which results in hindering the heat transfer into the tool and the generated heat is blocked in the workpiece. Therefore, the thermal effect is dominant which results in more tensile residual stresses.
- Nose radius: increasing the nose radius of the tool results in increasing the contact area between tool and workpiece which consequently results in more frictional heat generation and less plastic deformation (the pressure per unit area decreases). Therefore, more tensile residual stresses are induced by increasing the nose radius.
- Cutting speed: increasing cutting speed evacuates much heat through the chip and hence the workpiece is subjected to less heating. Therefore, the thermal effect (the main source of tensile residual stresses) is decreased.
- Feed rate: increasing the feed rate results in increasing the material removal rate and as a consequence the cutting forces are also increased, which consequently results in excessive heat generation and the cutting temperature is increased, and hence, the thermal effect is dominant which result in more surface tensile residual stresses.
- Cutting depth: increasing the cutting depth results in the same effect of increasing the feed rate, as the material removal rate increases and much heat is generated which results in more tensile residual stresses.

The Pearson correlation coefficient and the p value between the generated residual stresses and the different investigated factors are (0.194, 0.273, -0.100 , 0.652, and 0.533) and (0.440, 0.272, 0.694, 0.003, and 0.023) for coating condition, nose radius, cutting speed, feed rate and cutting of depth, respectively, which indicates the significant effect of the feed rate followed by the cutting depth on the induced residual stresses (with very low p value of 0.003,

and 0.023), while the coating condition, nose radius, and cutting speed have a mild correlation with the maximum generated temperature (with p value of 0.440, 0.272, and 0.694, which is greater than the significance level of 0.05). The same results can be observed from Fig. 6b that the cutting depth and the feed rate have a significant effect on the induced residual stresses compared with other investigated parameters.

4 Conclusion

This paper provides a comprehensive investigation of surface RSes, microstructure, and hardness induced in machined AISI 1035 steel alloy by turning. The effects of cutting conditions and parameters including cutting speed, feed rate, cutting depth, cutting tool coating condition, and cutting tool nose radius on the cutting temperature and cutting forces are also discussed. The experimental results have been analyzed using analysis of variance (ANOVA). Numerical simulations have been carried out using commercial machining software AdvantEdge. The obtained results revealed the significant effect of the cutting depth and the feed rate on the surface RSes. Moreover, an obvious correlation between cutting forces and the peak temperature in the machined workpiece as well as the induced surface RSes has been observed. The simulation results indicated that high heat rates of 1.5 KW/mm³ were generated during cutting process at cutting. Moreover, very high strain rates were observed in the cutting zone that reached 1500 s⁻¹ with peak plastic strain and Mises stress of 4 and 1000 MPa, respectively. The cutting force is much higher than passive and feed forces, and all of them are significantly affected by cutting depth followed by feed rate and cutting speed. The use of coated tools caused a remarkable increase in the workpiece temperature as the coating acted as a thermal barrier, leading to more heat transferred into the workpiece. The increase in cutting depth and feed rate resulted in the increase in the generated heat and consequently the residual stresses. Moreover, no significant change in the workpiece microstructure was observed during experiments as the maximum cutting temperature for all conducted experiments did not exceed the austenitizing temperature (830–860 °C). Finally, to get a compressive RSes state during turning and to avoid tensile RSes, the following recommendations should be considered:

- (i) Using uncoated tools so that more heat is transferred to the cutting tool rather than be blocked in the workpiece, the thermal effect is decreased which results in decreasing the tensile RSes.
- (ii) Using cutting tools with small nose radius to decrease the contact area between tool and workpiece which

consequently results in reducing frictional heat generation; so, the surface tensile RSEs are decreased.

- (iii) Increasing cutting speed as more heat is evacuated through chips and the thermal effects are decreased.
- (iv) Decreasing feed rate and cutting to decrease the material removal rate and as a consequence the cutting forces are also decreased, which consequently results in less heat generation and the decrease in cutting temperature which results in less surface tensile residual stresses.

So, for obtaining better surface integrity without affecting the material removal rate, it is recommended to increase the cutting speed and decrease both cutting depth and feed rate.

Acknowledgements This work was supported by the National Natural Science Foundation of China (E050902, E041604).

Compliance with ethical standards

Conflict of interest The authors declared that there is no conflict of interest.

References

1. Huang X-D, Zhang X-M, Ding H (2016) A novel relaxation-free analytical method for prediction of residual stress induced by mechanical load during orthogonal machining. *Int J Mech Sci* 115–116:299–309. <https://doi.org/10.1016/j.ijmecsci.2016.06.024>
2. Elajrami M, Miloud R, Milouki H, Boukhoulda FB (2016) Experimental investigation of the effect of double cold expansion on the residual stresses distribution and on the fatigue life of rivet hole. *J Braz Soc Mech Sci Eng* 38(8):2527–2532. <https://doi.org/10.1007/s40430-015-0381-x>
3. Yazdani Nezhad H, O'Dowd NP (2015) Creep relaxation in the presence of residual stress. *Eng Fract Mech* 138:250–264. <https://doi.org/10.1016/j.engfractmech.2015.03.037>
4. Ghosh S, Rana VPS, Kain V, Mittal V, Baveja SK (2011) Role of residual stresses induced by industrial fabrication on stress corrosion cracking susceptibility of austenitic stainless steel. *Mater Des* 32(7):3823–3831. <https://doi.org/10.1016/j.matdes.2011.03.012>
5. Hioki D, Diniz AE, Sinatora A (2013) Influence of HSM cutting parameters on the surface integrity characteristics of hardened AISI H13 steel. *J Braz Soc Mech Sci Eng* 35(4):537–553. <https://doi.org/10.1007/s40430-013-0050-x>
6. Devarajan N, Asundi MK, Somasundaram S (1984) Experimental method for predicting residual stresses due to turning in stainless steel. *Exp Tech* 8(8):22–26. <https://doi.org/10.1111/j.1747-1567.1984.tb01935.x>
7. Huang X, Sun J, Li J, Han X, Xiong Q (2013) An experimental investigation of residual stresses in high-speed end milling 7050-T7451 aluminum alloy. *Adv Mech Eng* 5:592659. <https://doi.org/10.1155/2013/592659>
8. Bobet JL, Masuda C (1996) Measurements of thermal residual stresses in SiC/Ti-15–3 composites. *J Therm Stress* 19(6):579–593. <https://doi.org/10.1080/01495739608946195>
9. Brunel F, Brunel J-F, Dufrénoy P, Demilly F (2013) Prediction of the initial residual stresses in railway wheels induced by manufacturing. *J Therm Stress* 36(1):37–55. <https://doi.org/10.1080/01495739.2012.720542>
10. Miguélez MH, Zaera R, Molinari A, Cheriguene R, Rusinek A (2009) Residual stresses in orthogonal cutting of metals: the effect of thermomechanical coupling parameters and of friction. *J Therm Stress* 32(3):269–289. <https://doi.org/10.1080/01495730802637134>
11. Elsheikh AH, Guo J, Lee K-M (2018) Thermal deflection and thermal stresses in a thin circular plate under an axisymmetric heat source. *J Therm Stress*. <https://doi.org/10.1080/01495739.2018.1482807>
12. Salahshoor M, Guo YB (2014) Finite element simulation and experimental validation of residual stresses in high speed dry milling of biodegradable magnesium–calcium alloys. *Int J Mech Sci* 80:153–159. <https://doi.org/10.1016/j.ijmecsci.2014.01.010>
13. Yang D, Liu Z, Ren X, Zhuang P (2016) Hybrid modeling with finite element and statistical methods for residual stress prediction in peripheral milling of titanium alloy Ti–6Al–4V. *Int J Mech Sci* 108–109:29–38. <https://doi.org/10.1016/j.ijmecsci.2016.01.027>
14. Dalewski R, Jachimowicz J, Pietrzakowski M (2010) Simulations of residual stresses in resistance spot welding process. *J Therm Stress* 33(9):843–857. <https://doi.org/10.1080/01495739.2010.482370>
15. Arrazola PJ, Kortabarria A, Madariaga A, Esnaola JA, Fernandez E, Cappellini C, Ulutan D, Özel T (2014) On the machining induced residual stresses in IN718 nickel-based alloy: experiments and predictions with finite element simulation. *Simul Model Pract Theory* 41:87–103. <https://doi.org/10.1016/j.simpat.2013.11.009>
16. Sherafatnia K, Farrahi GH, Mahmoudi AH, Ghasemi A (2016) Experimental measurement and analytical determination of shot peening residual stresses considering friction and real unloading behavior. *Mater Sci Eng A* 657:309–321. <https://doi.org/10.1016/j.msea.2016.01.070>
17. Sebastiani M, Sui T, Korsunsky AM (2017) Residual stress evaluation at the micro- and nano-scale: recent advancements of measurement techniques, validation through modelling, and future challenges. *Mater Des* 118:204–206. <https://doi.org/10.1016/j.matdes.2017.01.025>
18. Buj-Corral I, Vivancos-Calvet J, Setien I, San Sebastian M (2017) Residual stresses induced by honing processes on hardened steel cylinders. *Int J Adv Manuf Technol* 88(5):2321–2329. <https://doi.org/10.1007/s00170-016-8870-3>
19. Wang Z, Denlinger E, Michaleris P, Stoica AD, Ma D, Beese AM (2017) Residual stress mapping in Inconel 625 fabricated through additive manufacturing: method for neutron diffraction measurements to validate thermomechanical model predictions. *Mater Des* 113:169–177. <https://doi.org/10.1016/j.matdes.2016.10.003>
20. Çelik YH, Kilickap E, Güney M (2017) Investigation of cutting parameters affecting on tool wear and surface roughness in dry turning of Ti–6Al–4V using CVD and PVD coated tools. *J Braz Soc Mech Sci Eng* 39(6):2085–2093. <https://doi.org/10.1007/s40430-016-0607-6>
21. Bouffieux C, Pesci R, Boman R, Caillet N, Ponthot J-P, Habraken AM (2016) Comparison of residual stresses on long rolled profiles measured by X-ray diffraction, ring core and the sectioning methods and simulated by FE method. *Thin-Walled Struct* 104:126–134. <https://doi.org/10.1016/j.tws.2016.03.017>
22. Ghasemi AR, Mohammadi MM (2016) Residual stress measurement of fiber metal laminates using incremental hole-drilling technique in consideration of the integral method. *Int J Mech Sci* 114:246–256. <https://doi.org/10.1016/j.ijmecsci.2016.05.025>
23. James MN, Newby M, Doubell P, Hattingh DG, Serasli K, Smith DJ (2014) Weld residual stresses near the bimetallic interface in clad RPV steel: a comparison between deep-hole drilling and neutron diffraction data. *Nucl Eng Des* 274:56–65. <https://doi.org/10.1016/j.nucengdes.2014.03.042>

24. Sun Y, Luzin V, Daniel WJT, Meehan PA, Zhang M, Ding S (2017) Development of the slope cutting method for determining the residual stresses in roll formed products. *Measurement* 100:26–35. <https://doi.org/10.1016/j.measurement.2016.12.036>
25. Gadallah R, Tsutsumi S, Hiraoka K, Murakawa H (2015) Prediction of residual stresses induced by low transformation temperature weld wires and its validation using the contour method. *Mar Struct* 44:232–253. <https://doi.org/10.1016/j.marstruc.2015.10.002>
26. Foadian F, Carradó A, Pirling T, Palkowski H (2016) Residual stresses evolution in Cu tubes, cold drawn with tilted dies – Neutron diffraction measurements and finite element simulation. *Mater Des* 107:163–170. <https://doi.org/10.1016/j.matdes.2016.06.028>
27. Mishchenko A, Wu L, da Silva VK, Scotti A (2018) Analysis of residual stresses resulting from the surface preparation for X-ray diffraction measurement. *J Braz Soc Mech Sci Eng* 40(2):94. <https://doi.org/10.1007/s40430-018-1036-5>
28. Lee HH, Gangwar KD, Park K-T, Woo W, Kim HS (2017) Neutron diffraction and finite element analysis of the residual stress distribution of copper processed by equal-channel angular pressing. *Mater Sci Eng A* 682:691–697. <https://doi.org/10.1016/j.msea.2016.11.094>
29. Özel T, Ulutan D (2012) Prediction of machining induced residual stresses in turning of titanium and nickel based alloys with experiments and finite element simulations. *CIRP Ann Manuf Technol* 61(1):547–550. <https://doi.org/10.1016/j.cirp.2012.03.100>
30. Liu CR, Guo YB (2000) Finite element analysis of the effect of sequential cuts and tool–chip friction on residual stresses in a machined layer. *Int J Mech Sci* 42(6):1069–1086. [https://doi.org/10.1016/S0020-7403\(99\)00042-9](https://doi.org/10.1016/S0020-7403(99)00042-9)
31. Wu J, Han RD (2009) A new approach to predicting the maximum temperature in dry drilling based on a finite element model. *J Manuf Process* 11(1):19–30. <https://doi.org/10.1016/j.jmapro.2009.07.001>
32. Pawade RS, Joshi SS, Brahmankar PK (2008) Effect of machining parameters and cutting edge geometry on surface integrity of high-speed turned Inconel 718. *Int J Mach Tools Manuf* 48(1):15–28. <https://doi.org/10.1016/j.ijmactools.2007.08.004>
33. Capello E (2006) Residual stresses in turning: part II. Influence of the machined material. *J Mater Process Technol* 172(3):319–326. <https://doi.org/10.1016/j.jmatprotec.2005.10.009>
34. Tsuchida K, Kawada Y, Kodama S (1975) A study on the residual stress distributions by turning. *Bull JSME* 18(116):123–130. <https://doi.org/10.1299/jsme1958.18.123>
35. Gunnberg F, Escursell M, Jacobson M (2006) The influence of cutting parameters on residual stresses and surface topography during hard turning of 18MnCr5 case carburised steel. *J Mater Process Technol* 174(1–3):82–90. <https://doi.org/10.1016/j.jmatprotec.2005.02.262>
36. Saini S, Ahuja IS, Sharma VS (2013) Modelling the effects of cutting parameters on residual stresses in hard turning of AISI H11 tool steel. *Int J Adv Manuf Technol* 65(5):667–678. <https://doi.org/10.1007/s00170-012-4206-0>
37. Liu M, Takagi J-i, Tsukuda A (2004) Effect of tool nose radius and tool wear on residual stress distribution in hard turning of bearing steel. *J Mater Process Technol* 150(3):234–241. <https://doi.org/10.1016/j.jmatprotec.2004.02.038>
38. Outeiro JC, Dias AM, Jawahir IS (2006) On the effects of residual stresses induced by coated and uncoated cutting tools with finite edge radii in turning operations. *CIRP Ann Manuf Technol* 55(1):111–116. [https://doi.org/10.1016/S0007-8506\(07\)60378-3](https://doi.org/10.1016/S0007-8506(07)60378-3)
39. Yue C, Wang B, Liu X, Feng H, Cai C (2015) Adiabatic shear mechanisms for the hard cutting process. *Chin J Mech Eng* 28(3):592–598. <https://doi.org/10.3901/cjme.2015.0311.028>
40. Outeiro JC, Umbrello D, M'Saoubi R (2006) Experimental and numerical modelling of the residual stresses induced in orthogonal cutting of AISI 316L steel. *Int J Mach Tools Manuf* 46(14):1786–1794. <https://doi.org/10.1016/j.ijmactools.2005.11.013>
41. Kundrák J, Mamalis AG, Szabó G, Pálmai Z, Gyáni K (2016) Numerical examination of residual stresses developing during hard turning at different rake angles. *Int J Adv Manuf Technol*. <https://doi.org/10.1007/s00170-016-9229-5>
42. Leppert T, Peng RL (2012) Residual stresses in surface layer after dry and MQL turning of AISI 316L steel. *Prod Eng Res Dev* 6(4):367–374. <https://doi.org/10.1007/s11740-012-0389-3>
43. Berruti T, Lavello M, Gola MM (2009) Residual stresses on Inconel 718 turbine shaft samples after turning. *Mach Sci Technol* 13(4):543–560. <https://doi.org/10.1080/10910340903451472>
44. Cakir MC, Isik Y (2005) Finite element analysis of cutting tools prior to fracture in hard turning operations. *Mater Des* 26(2):105–112. <https://doi.org/10.1016/j.matdes.2004.05.018>
45. Xueping Z, Erwei G, Richard Liu C (2009) Optimization of process parameter of residual stresses for hard turned surfaces. *J Mater Process Technol* 209(9):4286–4291. <https://doi.org/10.1016/j.jmatprotec.2008.10.011>
46. Warren AW, Guo YB (2009) Characteristics of residual stress profiles in hard turned versus ground surfaces with and without a white layer. *J Manuf Sci Eng* 131(4):041004–041010. <https://doi.org/10.1115/1.3159046>
47. Liu CR, Mittal S (1996) Single-step superfinish hard machining: feasibility and feasible cutting conditions. *Robot Comput Integr Manuf* 12(1):15–27. [https://doi.org/10.1016/0736-5845\(95\)00029-1](https://doi.org/10.1016/0736-5845(95)00029-1)
48. Kara F, Aslantaş K, Çiçek A (2016) Prediction of cutting temperature in orthogonal machining of AISI 316L using artificial neural network. *Appl Soft Comput* 38:64–74. <https://doi.org/10.1016/j.asoc.2015.09.034>
49. Elsheikh AH, Sharshir SW, Abd Elaziz M, Kabeel AE, Guilan W, Haiou Z (2019) Modeling of solar energy systems using artificial neural network: a comprehensive review. *Sol Energy* 180:622–639. <https://doi.org/10.1016/j.solener.2019.01.037>
50. Elsheikh A, Showaib E, Asar A (2013) Artificial neural network based forward kinematics solution for planar parallel manipulators passing through singular configuration. *Adv Robot Autom* 2(106):2
51. Deng W, Zhang S, Zhao H, Yang X (2018) A novel fault diagnosis method based on integrating empirical wavelet transform and fuzzy entropy for motor bearing. *IEEE Access* 6:35042–35056. <https://doi.org/10.1109/ACCESS.2018.2834540>
52. Zhao H, Sun M, Deng W, Yang X (2017) A new feature extraction method based on EEMD and multi-scale fuzzy entropy for motor bearing. *Entropy* 19(1):14
53. Deng W, Xu J, Zhao H (2019) An improved ant colony optimization algorithm based on hybrid strategies for scheduling problem. *IEEE Access* 7:20281–20292. <https://doi.org/10.1109/ACCESS.2019.2897580>
54. Deng W, Zhao H, Zou L, Li G, Yang X, Wu D (2017) A novel collaborative optimization algorithm in solving complex optimization problems. *Soft Comput* 21(15):4387–4398. <https://doi.org/10.1007/s00500-016-2071-8>
55. Elaziz MA, Elsheikh AH, Sharshir SW (2019) Improved prediction of oscillatory heat transfer coefficient for a thermoacoustic heat exchanger using modified adaptive neuro-fuzzy inference system. *Int J Refrig* 102:47–54. <https://doi.org/10.1016/j.ijrefrig.2019.03.009>
56. Deng W, Zhao H, Yang X, Xiong J, Sun M, Li B (2017) Study on an improved adaptive PSO algorithm for solving multi-objective gate assignment. *Appl Soft Comput* 59:288–302. <https://doi.org/10.1016/j.asoc.2017.06.004>

57. Elsheikh AH, Abd Elaziz M (2019) Review on applications of particle swarm optimization in solar energy systems. *Int J Environ Sci Technol* 16(2):1159–1170. <https://doi.org/10.1007/s13762-018-1970-x>
58. Deng W, Yao R, Zhao H, Yang X, Li G (2019) A novel intelligent diagnosis method using optimal LS-SVM with improved PSO algorithm. *Soft Comput* 23(7):2445–2462. <https://doi.org/10.1007/s00500-017-2940-9>
59. Oliva D, Abd Elaziz M, Elsheikh AH, Ewees AA (2019) A review on meta-heuristics methods for estimating parameters of solar cells. *J Power Sources* 433:126683
60. Wyatt JE, Berry JT (2006) A new technique for the determination of superficial residual stresses associated with machining and other manufacturing processes. *J Mater Process Technol* 171(1):132–140. <https://doi.org/10.1016/j.jmatprotec.2005.06.067>
61. García Navas V, Gonzalo O, Bengoetxea I (2012) Effect of cutting parameters in the surface residual stresses generated by turning in AISI 4340 steel. *Int J Mach Tools Manuf* 61:48–57. <https://doi.org/10.1016/j.ijmachtools.2012.05.008>
62. Caruso S, Umbrello D, Outeiro JC, Filice L, Micari F (2011) An experimental investigation of residual stresses in hard machining of AISI 52100 steel. *Procedia Eng* 19:67–72. <https://doi.org/10.1016/j.proeng.2011.11.081>
63. Jang DY, Watkins TR, Kozaczek KJ, Hubbard CR, Cavin OB (1996) Surface residual stresses in machined austenitic stainless steel. *Wear* 194(1):168–173. [https://doi.org/10.1016/0043-1648\(95\)06838-4](https://doi.org/10.1016/0043-1648(95)06838-4)
64. Capello E, Davoli P, Bassanini G, Bisi A (1999) Residual stresses and surface roughness in turning. *J Eng Mater Technol* 121(3):346–351. <https://doi.org/10.1115/1.2812385>
65. Abboud E, Attia H, Shi B, Damir A, Thomson V, Mebrahtu Y (2016) Residual stresses and surface integrity of Ti-alloys during finish turning—guidelines for compressive residual stresses. *Procedia CIRP* 45:55–58. <https://doi.org/10.1016/j.procir.2016.02.069>
66. Madariaga A, Kortabarria A, Hormaetxe E, Garay A, Arrazola PJ (2016) Influence of tool wear on residual stresses when turning Inconel 718. *Procedia CIRP* 45:267–270. <https://doi.org/10.1016/j.procir.2016.02.359>
67. Li W, Withers PJ, Axinte D, Preuss M, Andrews P (2009) Residual stresses in face finish turning of high strength nickel-based superalloy. *J Mater Process Technol* 209(10):4896–4902. <https://doi.org/10.1016/j.jmatprotec.2009.01.012>
68. Javid A, Rieger U, Eichlseder W (2008) The effect of machining on the surface integrity and fatigue life. *Int J Fatigue* 30(10–11):2050–2055. <https://doi.org/10.1016/j.ijfatigue.2008.01.005>
69. Vigraman T, Narayanasamy R, Ravindran D (2012) Microstructure and mechanical property evaluation of diffusion-bonded joints made between SAE 2205 steel and AISI 1035 steel. *Mater Des* 35:156–169. <https://doi.org/10.1016/j.matdes.2011.09.063>
70. John EB (2007) Handbook of comparative world steel standards, 4th edn. ASTM International, Mayfield
71. Noyan IC, Cohen JB (1987) Determination of strain and stress fields by diffraction methods. In: Residual stress: measurement by diffraction and interpretation. Springer, New York, pp 117–163. https://doi.org/10.1007/978-1-4613-9570-6_5
72. Ma J, Duong NH, Lei S (2015) Numerical investigation of the performance of microbump textured cutting tool in dry machining of AISI 1045 steel. *J Manuf Process* 19:194–204. <https://doi.org/10.1016/j.jmapro.2014.10.001>
73. Cascón I, Sarasua JA (2015) Mechanistic model for prediction of cutting forces in turning of non-axisymmetric parts. *Procedia CIRP* 31:435–440. <https://doi.org/10.1016/j.procir.2015.03.084>
74. Capello E (2005) Residual stresses in turning: part I: influence of process parameters. *J Mater Process Technol* 160(2):221–228. <https://doi.org/10.1016/j.jmatprotec.2004.06.012>
75. Elsheikh AH, Guo J, Huang Y, Ji J, Lee K-M (2018) Temperature field sensing of a thin-wall component during machining: numerical and experimental investigations. *Int J Heat Mass Transf* 126:935–945. <https://doi.org/10.1016/j.ijheatmasstransfer.2018.06.006>
76. Zhang S, Ding T, Li J (2012) Microstructural alteration and microhardness at near-surface of AISI H13 steel by hard milling. *Mach Sci Technol* 16(3):473–486

Publisher's Note Springer Nature remains neutral with regard to jurisdictional claims in published maps and institutional affiliations.